



Contents lists available at ScienceDirect

Computers & Fluids

journal homepage: www.elsevier.com/locate/complfluid



Starting jet flows in a three-dimensional channel with larynx-shaped constriction

Rüdiger Schwarze*, Willy Mattheus, Jens Klostermann, Christoph Brücker

Institut für Mechanik und Fluidodynamik, TU Bergakademie Freiberg, Lampadiusstr. 4, 09596 Freiberg, Germany

ARTICLE INFO

Article history:
Received 2 June 2009
Received in revised form 21 March 2011
Accepted 31 March 2011
Available online xxxx

Keywords:

Glottal airflow
Elliptic jet
Instability
Jet breakdown
Numerical simulation
Larynx-shaped channel
Starting jet flow
Numerical model
Validation

ABSTRACT

A numerical model for the three-dimensional starting jet flow in a channel with a static larynx-shaped constriction is presented. Detailed resolution of this kind of jet flow is necessary in order to understand the complex coupling between flow and acoustics in the process of human phonation. The numerical model is based on the equation of continuity and the Navier–Stokes equations. The investigations are done with the open source CFD package OpenFOAM. Numerical simulations are performed for a square-sectioned channel geometry, which is constricted with a fixed shape conforming to the fully opened human glottis. Time-dependent inflow boundary conditions are applied in order to model transient glottal flow rates. The setup of the numerical simulations corresponds to the configuration of a model experiment in order to allow detailed validation. The numerical results are in good agreement with the experimental data, when the near-wall region in the glottal gap is adequately resolved by the numerical grid. The results illustrate the complex interactions between the jet flow and the surrounding vortices.

© 2011 Published by Elsevier Ltd.

1. Introduction

Human voice is produced by the pulsating airflow generated during the self-sustained oscillations of the vocal folds. Actually, the physics of this phenomenon with emphasize on the interactions between the vocal folds oscillation, the aerodynamics of the airflow and the acoustics of the generated sound is a highly active field of interdisciplinary research, see e.g. [1]. Fluid mechanics research is done with experimental models or with numerical simulations. Among others, some important effects which have been studied in the past by means of computational fluid dynamics (CFD) are flow separation in the glottis [2,3], Coanda effect [4,5], intraglottal pressure distribution [3,4,6], glottal airflow rate [1,3,7], pulsating air jet flows [8–10] and supraglottal jet turbulence [5].

The nonacoustic fluid motion of the air in the glottis provides a source of sound, with the monopole source associated to the pulsating air flow and dipole as well as quadrupole source terms which arise from the mutual interactions of vortical structures and the supraglottal jet with the walls. It is generally accepted that flow separation in the glottis has a major effect on the pressure field and the jet flow in the supraglottal region, see e.g. [2]. There are several papers which investigate flow separation in the glottis by means of numerical simulations with lower-dimensional

numerical models, e.g. [1,3]. These models have special treatments for the correct prediction of flow separation. On the contrary the transient three-dimensional supraglottal flow field consisting of the jet and the induced vortex structures has been studied only experimentally so far [11–13]. Previous numerical studies of the three-dimensional supraglottal flow have been focused on the laryngeal jet during aspiration, e.g. [14,15].

In the paper, we investigate the starting glottal jet downstream of a rigid glottis-shaped constriction. The flow is similar but not identical to the well-known starting round jet flow, which kinematics and dynamics has been investigated in detail in the past years [16–21]. Gharib and coworkers [16–18,20] introduced the formation number of a vortex ring which is generated through an impulsively starting jet. The formation number characterizes the separation of the vorticity field of the leading vortex from the trailing jet [16]. The formation number of a starting jet flow can be varied by the modification of jet acceleration scenario or the orifice shape [19]. By the inspection of the vortex dynamics, Krueger and Gharib [20] found that impulse transfer from the starting round jet to the surrounding fluid is maximized at the formation number. Due to the symmetry of the problem, it is also possible to describe the pinch-off process of the leading vortex from the jet by analytical models [18,21].

Our paper presents a fully three-dimensional numerical model of the starting glottal jet flow in order to study the transient flow downstream of the glottis-shaped constriction in detail. Numerical simulations are carried out for a square-sectioned channel with a glottis-shaped constriction.

* Corresponding author. Tel.: +49 3731 392486; fax: +49 3731 393455.
E-mail address: Ruediger.Schwarze@imfd.tu-freiberg.de (R. Schwarze).

The geometry of the numerical model follows the setup of the experimental model of Triep et al [11]. The numerical model is implemented in the open CFD library OpenFOAM. A detailed description of the numerical model is given. The numerical simulations are done in the absence of fluid-structure interactions. A comparison of the numerical results with corresponding flow data is given.

The scope of the paper is to resolve details of the kinematics and dynamics of the starting glottal jet. Therefore the basic mechanisms of the transient development, i.e. flow separation, formation of the leading vortex and interactions between the leading vortex and the trailing jet are investigated.

The paper presents a status report of an ongoing research project. Systematic investigations of oscillating airflows in a glottis-shaped channel will be given in a separate paper.

2. Numerical model

2.1. Glottal channel

The geometry parameters of the numerical model corresponds to a water model experiment of the flow in a square-sectioned channel with a glottis-shaped constriction in order to allow validation by comparison with corresponding flow data. Photographs which show the setup of the water model are given in Fig. 1.

The experimental setup is in principle a U-shaped channel composed of a test section with a vertical liquid column at each end, see Fig. 1a. All channel components are made of Perspex in order to have full optical accessibility into the transparent liquid medium. Included into the test section is the non-transparent glottis-shaped constriction, Fig. 1b. The glottis geometry is replicated by two cams, which model the upper and the lower vocal fold. Each of the cams is pivoted in a wedge, then covered with a silicone membrane and arranged vis-a-vis in the test section of the channel. The geometric data for the glottis is given in Table 1.

Note that this cam model is a 3:1 scale-up of a typical human glottis. Flow is induced by imposing a pressure head across the model glottis through a difference in the up- and downstream liquid column heights. According to the fluid dynamical similarity laws and considering water as the working medium, the pressure head in the model is of half the value compared to the value in natural phonation and velocities are of the order of 1 m/s. This fluid dynamical time scale allows a better way to visualize the glottal jet in the experiment and to extract velocity data of the flow field by means of Particle-Image Velocimetry. More details of the water model experiment are given by Triep et al. [11].

Fig. 2 gives the geometry of computational domain, which is used in the numerical simulations. The computational domain encompasses the test section of the water model. It is expected, that the homogeneous flow upstream of the glottis has little influ-

Table 1

Characteristic parameters of the glottal constriction in the numerical model according to Triep et al. [11].

Parameter	Value
α	45°
β	80°
w^{max}	8 mm
H	60 mm
W	60 mm

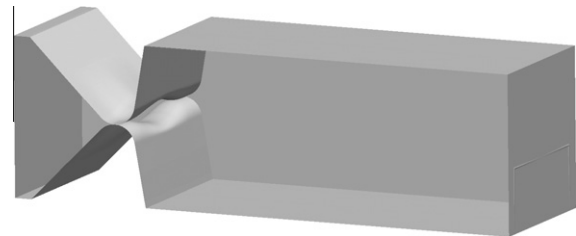
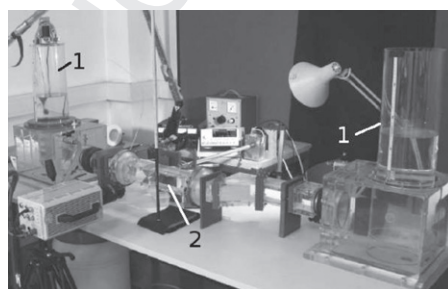


Fig. 2. Geometry of the computational domain.

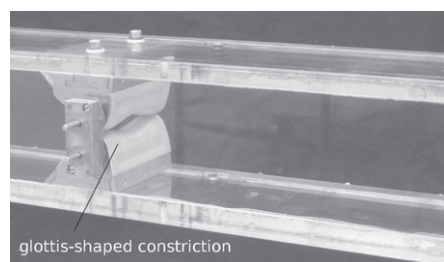
ence on the structure of the supraglottal flow. Hence, the subglottal flow region is reduced to a short inflow neck on the left-hand side of the glottal constriction. The global dimensions of the computational domain are $L \times H \times W = 200 \text{ mm} \times 60 \text{ mm} \times 60 \text{ mm}$ (due to the 3:1 upscaling). The boundaries of the computational domain correspond to the inner contour of the test section (upper, lower, front and back walls) with additional inlet (left) and outlet (right) boundary.

Details of the computational domain with the channel and the glottal constriction are sketched in Fig. 3. The characteristic parameters of the constriction are the angles α and β , the maximum opening width w^{max} of the glottis and finally the height H and width W of the supraglottal channel. The dimensions of these parameters which are implemented in the computational grids are given in Table 1. With H and W , the hydraulic equivalent diameter D of the channel becomes 60 mm.

The characteristic parameters of the glottal constriction correspond identically to the parameters of the water model experiment of Triep et al. [11]. A discussion of the similarity of the flow in the experiment and the numerical simulations with the real flow in the human glottis is also given by Triep et al. [11]. In summary, the flows in the numerical simulations meet Reynolds and Strouhal similarity to the real laryngeal flows. Since the Mach number is less than 0.1, the flow can be treated as incompressible. Therefore significant structures of the laryngeal flow can be resolved by incompressible flows in a water model experiment or a corresponding numerical simulation, respectively.



(a) U-shaped channel with liquid columns (1) and test section (2).



(b) Zoom into the test section with cam model of the glottis.

Fig. 1. Water model of the glottal channel with glottis-shaped constriction.

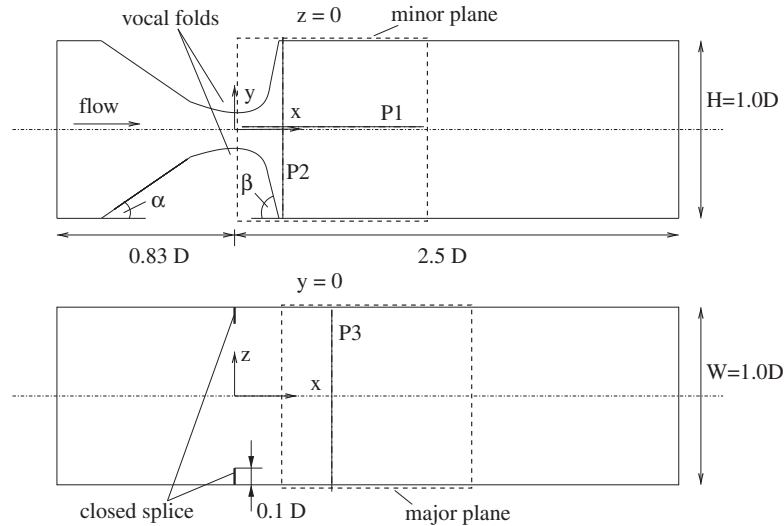


Fig. 3. Geometry of the computational model for the glottal channel, major and minor plane, baselines P1, P2 and P3 are employed for inspection of flow data.

2.2. Measurements of the starting flow

In the experiments, the starting jet flow is generated by a jump-like opening of a valve in the pressure chamber connected to the subglottal channel. The pressure head is realized by a difference of the sub- and supraglottal water level heights, which is hold by a magnetic valve above the subglottal water level. The flow is started by the opening of the magnetic valve. Then, the flow rate Q starts from zero and reaches the maximum value after a period $\tau = 700$ ms because the sub- and supraglottal water level heights are balanced by the flow.

In the water model experiment, the time-dependent behavior of Q is recorded. PIV measurements have been carried out in the major and minor planes indicated in Fig. 3. The major plane reaches from $(x,z) = (0.2 D, -0.5 D)$ (lower left corner) to $(x,z) = (1.2 D, 0.5 D)$ (upper right corner). The minor plane reaches from $(x,y) = (0, -0.5 D)$ (lower left corner) to $(x,y) = (1.0 D, 0.5 D)$ (upper right corner).

The measurements have been repeated in order to obtain an ensemble of 10 realizations of the starting flow. From these measurements, ensemble averaged flow data are available. Later, vorticity fields from the experiment and the simulations are compared in the major and minor plane. Additionally, velocity profiles are compared along baselines P1 (x -axis), P2 ($x = 0.2 D, z = 0$) and P3 ($x = 0.5 D, y = 0$).

2.3. Governing equations and model assumptions

The incompressible flow in the glottal channel will exhibit a transitional behavior. Starting with completely laminar flow conditions, the flow becomes super-critical in the glottal region after some acceleration. Then transition to turbulence is observed downstream of the glottal constriction. The CFD model which should describe both the laminar and the turbulent flow regime is based on the Navier–Stokes equations for incompressible, viscid flows

$$\frac{\partial u_j}{\partial x_j} = 0 \quad (1)$$

$$\frac{\partial u_i}{\partial t} + u_j \frac{\partial u_i}{\partial x_j} = -\frac{1}{\rho} \frac{\partial p}{\partial x_i} + \nu \frac{\partial^2 u_i}{\partial x_j^2} \quad (2)$$

in combination with high-order numerical discretisation schemes. In Eqs. (1) and (2) u is the flow velocity and p is the pressure. The

material parameters of water are density $\rho = 10^3 \text{ kg/m}^3$ and kinematic viscosity $\nu = 10^{-6} \text{ m}^2/\text{s}$. The numerical schemes are described in detail in the next sections.

The numerical setup is assumed to provide a blending between a direct computation of the laminar flow regions and an implicit Large-Eddy Simulation (ILES) [22,23] for the transitional and the turbulent flow regions. ILES has been successfully applied in numerical simulations of transitional square jet flows [24] and decaying vortex flows [25]. In these studies, the behavior of large coherent structures around non-circular jets and energy transfer from the large coherent to the turbulent structures have been resolved in good agreement with experimental observations and direct numerical simulations, respectively. These effects dominate the flow downstream of the glottal constriction, too. Therefore the ILES approach is assumed to work well in the present problem.

2.4. Numerical scenario and boundary conditions

As discussed above, the focus of the numerical investigations is the correct description of the developing supraglottal flow structures, namely the starting supraglottal jet, the vortex structures and their interactions. Because fluid-structure interactions in the glottis are neglected in this first approach, the glottal opening is kept fixed throughout the simulations. Therefore, the numerical scenario is based on a time-dependent behavior of the flow rate $Q(t)$ in the channel, which has been measured in the water model experiment.

A velocity inlet condition $\underline{u}^{in} = (u^{in}(t), 0, 0)$ for the numerical simulations is derived from $Q(t)$. The velocity inlet drives the global flow in the laryngeal channel. The time-dependent velocity function $u^{in}(t)$ is shown in Fig. 4. The Reynolds number Re based on the hydraulic equivalent diameter $d = 8.7$ mm of the glottis gap is also given in the figure, with a maximum value around $Re \approx 8800$. A pressure outlet with a gauge pressure $p^{out} = 0$ Pa with respect to the static pressure head of the downstream liquid column is applied at the outflow of the channel. Finally, the no-slip condition $\underline{u}^{wall} = 0 \text{ m/s}$ is applied at the rigid walls of the domain.

From the experiments, it is found that the turbulence intensity in the subglottal domain upstream of the glottal constriction is far below 1%. Therefore an explicit velocity fluctuation is not prescribed at the inlet boundary. The transition of the flow occurs downstream of the glottis.

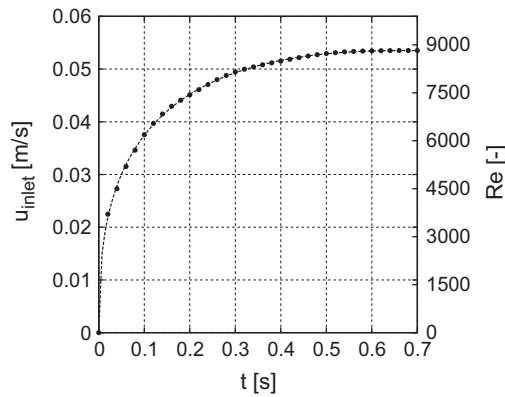
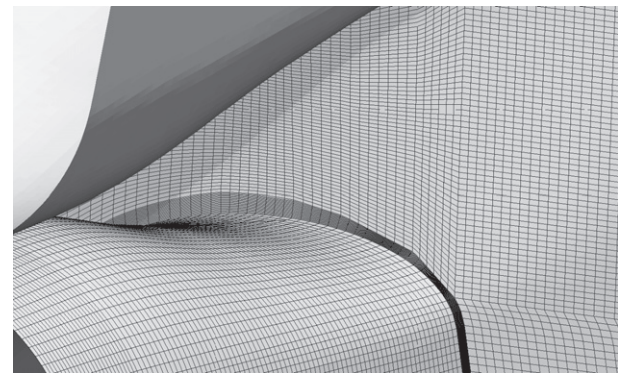
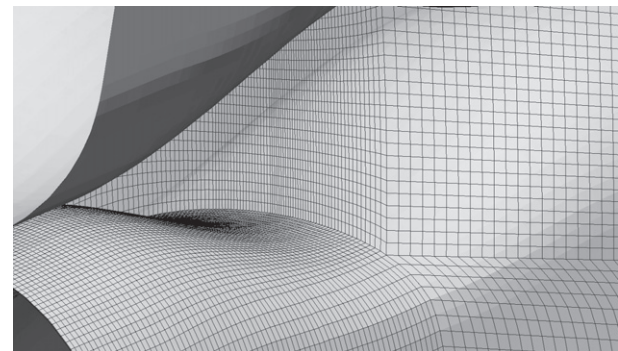


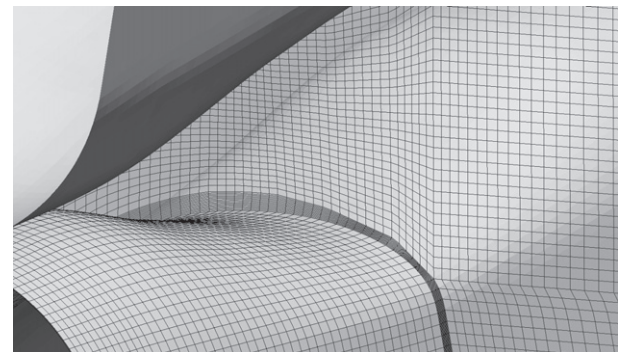
Fig. 4. Inlet velocity function $u_{inlet}^m(t)$ applied in the simulations, dots indicate measured values from the experiment.



(a) fine, with wall refinement - FMWR



(b) fine, without wall refinement - FM



(c) coarse, with wall refinement - WR

Fig. 5. Computational grids: near-wall treatment in the glottis.

244 2.5. Computational grid

245 A block-structured approach is employed in order to mesh the
246 computational domain in Fig. 2. Here, attention has been paid to
247 a regular resolution of the overall flow domain, which is discret-
248 ized into grids with three different grid resolutions, Fig. 5. The first
249 grid (fine mesh with wall resolution - FMWR) consists of about
250 5,000,000 grid cells and special attention has been paid for a fine
251 resolution of the near-wall cells in the glottal gap, Fig. 5a.

252 Here, the dimensionless wall distance of the wall-nearest node
253 is $y^+ = O(1)$ almost everywhere in the glottal opening. In order to
254 achieve $y^+ = O(1)$, the values of y^+ in the wall-adjacent cells in the
255 glottis have been checked after test calculations. If necessary, the
256 near-wall grid has been re-arranged until $y^+ = O(1)$ is fulfilled
257 throughout the complete simulation period.

258 The second grid (fine mesh without wall resolution - FM) con-
259 sists of 3.000.000 grid cells. In the glottis, it has approximately the
260 same grid resolution in the core flow region as grid FMWR, but there
261 is no near-wall grid refinement in the glottal gap, Fig. 5b. The third
262 grid (coarse mesh with wall resolution - WR) consists of only
263 1,000,000 grid cells, with a similar near-wall grid resolution than
264 in grid FMWR but a less dense spacing in the core flow region, Fig. 5c.

265 With the near-wall grid refinement in grids FMWR and WR, we
266 assume that two important structures of the flow are sufficiently
267 resolved:

- 268 1. the flow separation line at the diverging part of the glottal
- 269 constriction,
- 270 2. the velocity distribution in the separating laminar boundary
- 271 layers, which determine the velocity distribution in the free
- 272 shear layers of the jet.

273 Special attention has been paid to the meshing of the glottal
274 constriction. Here geometric singularities result from the touching
275 of the two curved faces of the lower and the upper vocal fold, see
276 Fig. 6b. Meshing of this part is crucial but high mesh quality has to
277 be maintained due to the developing shear layers in this region.
278 Therefore the geometry is slightly modified at the region of touch-
279 ing faces. A tiny closed splice of 0.1 mm height and 6 mm length is
280 introduced in the outer part of the glottal gap, Fig. 6b. The location
281 of the closed splice is indicated in Fig. 3. With the closed splice,
282 block-structured meshing is possible in this region.

284 2.6. Numerics

285 Eqs. (1) and (2) are integrated with the CFD library OpenFOAM
286 [26]. OpenFOAM uses the finite-volume method in cell-centered

287 formulation in order to solve systems of partial differential equa-
288 tions on 3D block-structured or unstructured meshes. OpenFOAM
289 has been already successfully employed in the context of both lam-
290 inar and ILES flow computations [25,28].

291 A TVD scheme with a flux limiter function $\psi(r) = \max[0, \min(2 \cdot$
292 $r, 1)]$ [27] is employed for interpolation of the convective flux terms
293 in the simulations. The smoothness parameter r is defined by the
294 ratio of consecutive gradients. The choice of the TVD scheme is
295 in line with the findings of Grinstein et al. [29], who note that
296 TVD schemes with local constraints should be preferred in the con-
297 text of ILES.

298 The 2nd order central differencing scheme (CDS) is used for the
299 discretization of the diffusive fluxes. Two different schemes are
300 employed for time integration of Eqs. (1) and (2): a first order scheme
301 (annotation CNE in the figures in Section 3) which blends the Crank-
302 Nicolson scheme with a weighting factor of 0.8 and the Euler impli-
303 cit scheme with a weighting factor of 0.2 and the second-order
304 three-level backward differencing scheme (annotation BW). Four

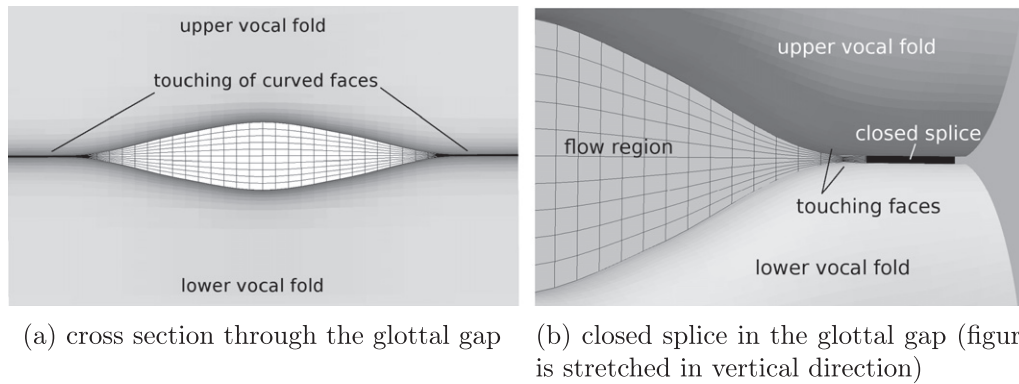


Fig. 6. Computational grid near the vocal folds (coarsened illustration of the grid in the flow region).

305 different time-step sizes $\Delta t_1 = 20 \mu s, \Delta t_2 = 10 \mu s, \Delta t_3 = 5 \mu s$ and
306 $\Delta t_4 = 2.5 \mu s$ are employed in the simulations.

307 The blending has been introduced because the combination of
308 the TVD, CDS and pure Crank-Nicolson schemes was found to be
309 only marginally stable in the simulations. During the transition
310 to turbulence, increasing high-frequency nonlinearities have led
311 to diverging solution behavior. Typically artificial dissipation
312 should be increased in the convective terms in order to circumvent
313 these problems. However this would influence the effect of the
314 TVD scheme and therefore the performance of the ILES approach.
315 Therefore we employ the blended time integration scheme in order
316 to stabilize the solution behavior. Due to the small time-step, the
317 1st order CNE scheme should be acceptable, which will be proven
318 by comparison with results from the BW simulations.

319 Mass conservation is enforced with the transient PISO algo-
320 rithm [30] with a collocated arrangement of pressure and velocity.
321 The formulation of the algorithm is in line with the Rhie and Chow
322 correction [31] in order to avoid non-physical oscillations in the
323 flow variables.

324 The pressure equation is solved with an algebraic multi-grid
325 solver with line Gauss-Seidel smoothing. The solver operates in
326 the sawtooth cycle with a summation operator for restriction and
327 an injection operator for prolongation. The momentum equations
328 are solved with the biconjugate gradient algorithm of Fletcher
329 [32], where incomplete LU decomposition is used for precondition-
330 ing the system.

331 The residual errors per time-step are of the order 10^{-7} for the
332 momentum equation and of the order of 10^{-8} for the pressure
333 equation.

334 The simulations have been carried out on the high performance
335 computers SGI Altix 4700 (featured with 1024 dual-core Intel Itanium
336 processors) and PC farm Deimos (724 heterogeneous compute
337 nodes featured with 1, 2 or 4 AMD Opteron Dual Core CPUs)
338 at the Center for Information Services and High Performance Com-
339 puting (ZIH) of the TU Dresden. For parallel computing, the grids
340 have been divided into 64, 96 or 128 partitions due to the METIS
341 method [33,34], respectively.

3. Results

3.1. Transient flow structure

344 The development of the elliptic jet in the supraglottal channel
345 can be visualized by regions of concentrated vorticity $\underline{\Omega} = \nabla \times \underline{u}$.
346 Fig. 7 gives characteristic snapshots from the ensemble-averaged
347 PIV measurements and the CFD simulations. The subfigures show
348 the major plane where important structures of the flow field are
349 indicated by the amplitude $\|\underline{\Omega}_y\|$ of the y component of $\underline{\Omega}$. The loca-

305 tions of the major and the minor plane are indicated in Fig. 3,
306 respectively. The scale of $\|\underline{\Omega}_y\|$ is given in sub Fig. 7c. The jet flow
307 direction is indicated by the arrow (a).
308

309 It can be seen that the leading vortex ring, which is intersected
310 by the major plane in (b), penetrates the quiescent fluid in the
311 supraglottal region. The stretched regions of large vorticity ampli-
312 tudes (c) are expected to represent the shear layers of the develop-
313 ing supraglottal jet flow, whereas compact regions of large
314 vorticity should correspond to cross sections through vortex tubes.
315

316 Figs. 8 and 9 show the development of the supraglottal jet flow
317 which is observed in the PIV measurements and in the numerical
318 simulations on grid FMWR. Fig. 8 displays the major plane with
319 the amplitude of the y component, Fig. 9 displays the minor plane
320 with the amplitude of the z component of $\underline{\Omega}$.

321 As a dominating effect, axis switching is observed in the exper-
322 iment as well as in the numerical simulation: In the developing jet,
323 the jet width w_z in the major plane decreases strongly down-
324 stream of the constriction, Fig. 8a and c, whereas the jet width w_y in
325 the minor plane is slightly increased, Fig. 9a and b. These observa-
326 tions are in agreement with the findings of Hussain and Husain [35,36]
327 for developing elliptic jets.

328 In the ensemble-averaged data from the PIV measurements, the
329 flow structures are obviously blurred. We assume that the jet shear
330 layers in the experiment are excited by some small-scale distur-
331 bances in the glottal region due to small background noise in the
332 experiments. Additionally small displacements between the indi-
333 vidual realizations of the ensemble may be responsible for the
334 blurring of the PIV data.

335 However, besides the small differences the overall development
336 of the starting elliptic jet agrees well in experiment and numerical
337 simulation.

338 The effects of the near-wall grid refinement is visualized in Figs.
339 10 and 11, where the jet development in the minor (Fig. 10) and
340 the major plane (Fig. 11) are compared for the three grids (i)
341 FMWR, (ii) FM and (iii) WR. It is evident, that the jet shape, the
342 axis switching (with the increase and the decrease of the jet minor
343 and major axis) and the transition to turbulence are similar resolved on
344 the two grids FMWR and WR with wall refinement.

345 On the contrary, these phenomena are resolved in different
346 mode on grid FM without wall refinement. Especially, the increase
347 and the decrease of the jet minor and major axis are strongly over-
348 estimated in comparison with the experimental findings in Figs. 8
349 and 9. Consequently, the stronger deceleration of the mean flow of
350 the elliptic jet induces a higher turbulence intensity downstream
351 of the trailing edge of the jet.

352 The influence of the time discretization on the flow resolution is
353 visualized in Fig. 12. Here, simulation results which are obtained
354 with different time integration schemes (CNE and BW) as well as
355 different time-step sizes (Δt_2 and Δt_3) are compared. Obviously
356

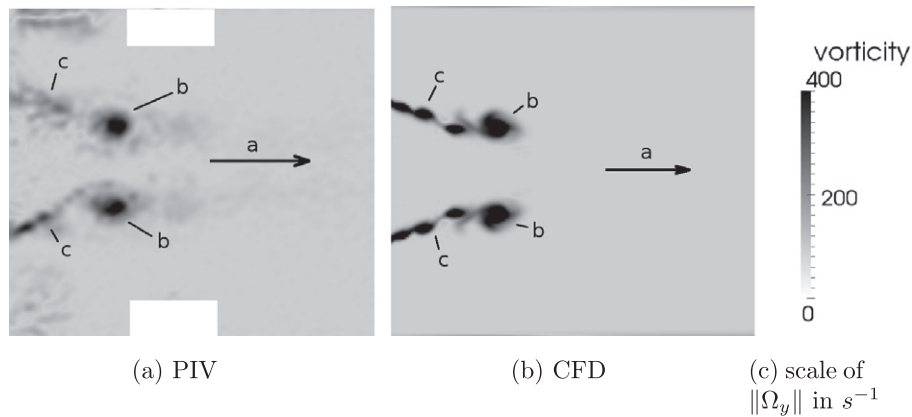


Fig. 7. Jet development in the major plane, main characteristics indicated by $\|\Omega_y\|$: (a) flow direction, (b) leading vortex, (c) jet shear layers.

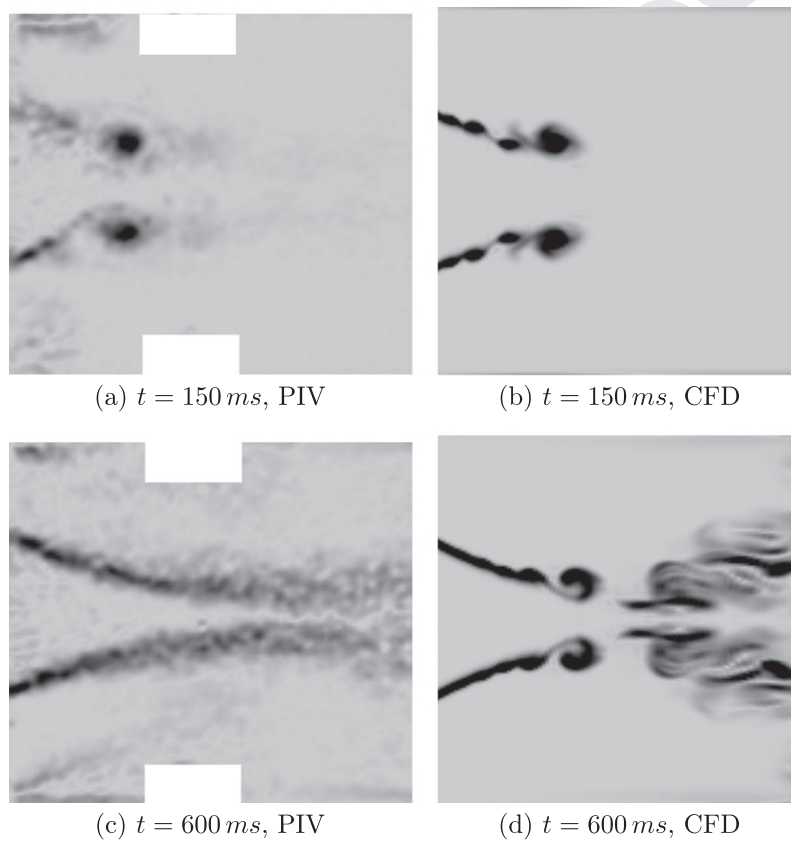


Fig. 8. Jet development in the major plane, indicated by $\|\Omega_y\|$ with the scale in Fig. 7c.

399 the influence of the time discretization on a specific grid is much
400 smaller than the previously discussed impact of the grid on the
401 quality of flow resolution.

402 3.2. Velocity profiles

403 For a more quantitative comparison between the different
404 numerical results and the experimental measurements, profiles
405 of the velocity in x -direction $u(x/H)$ along the baselines P1, P2
406 and P3, see Fig. 3, are inspected.

407 Fig. 13 shows an example of the velocity profile from the
408 numerical simulation with grid FMWR at flow time $t = 450$ ms. In
409 the velocity profile, two different regions can be identified. Region
410 (i) gives the nearly constant velocity in the developed core of the

elliptic jet. Region (ii) is dominated by the large coherent vortex
411 structures, which have been developed from the jet shear layers. 412
The coherent structures reach the jet centerline around $x/H = 0.6$ 413
where the two shear layers come close to each other. Downstream 414
of this point, they induce an acceleration and deceleration of the jet 415
axial velocity similar to a wave train. 416

417 Fig. 14 compares the numerical (FMWR, FM, WR) and experi- 418
mental (PIV) velocity profiles at baseline P1 for four different flow 419
times t . The experimental velocity profile gives the ensemble-aver- 420
aged PIV data. Here error bars indicate the uncertainty in the re- 421
ported measurements.

422 In all subfigures, the numerical simulations on grids FMWR and 423
WR fit reasonably to the experimental measurements for $x \leq 0.6$. 424
Downstream of this point, there are larger differences between

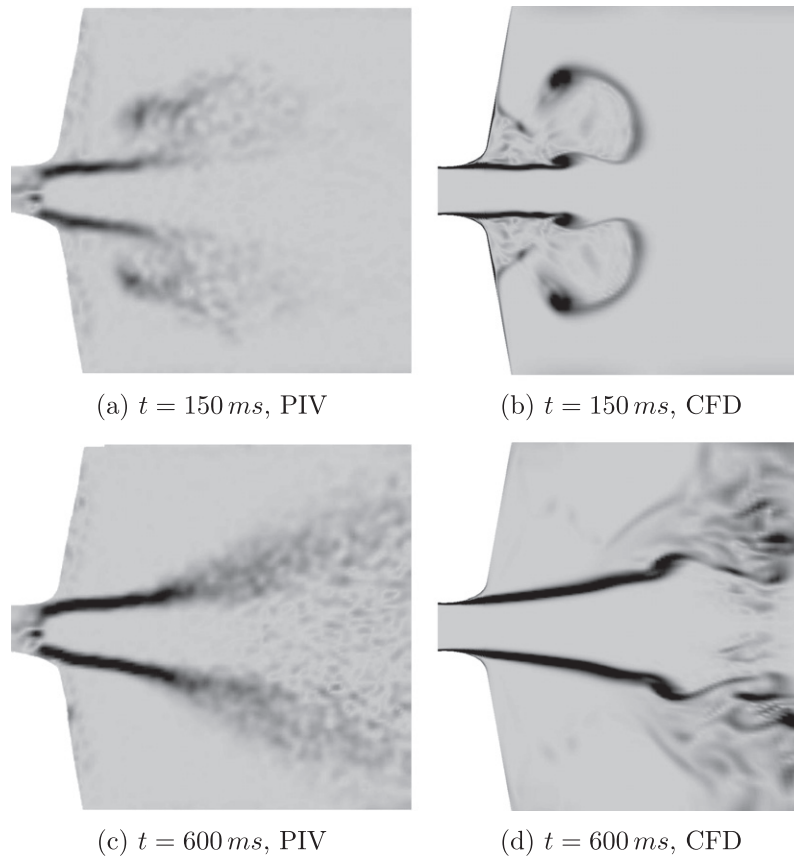


Fig. 9. Jet development in the minor plane, indicated by $\|\Omega_z\|$ with the scale in Fig. 7c.

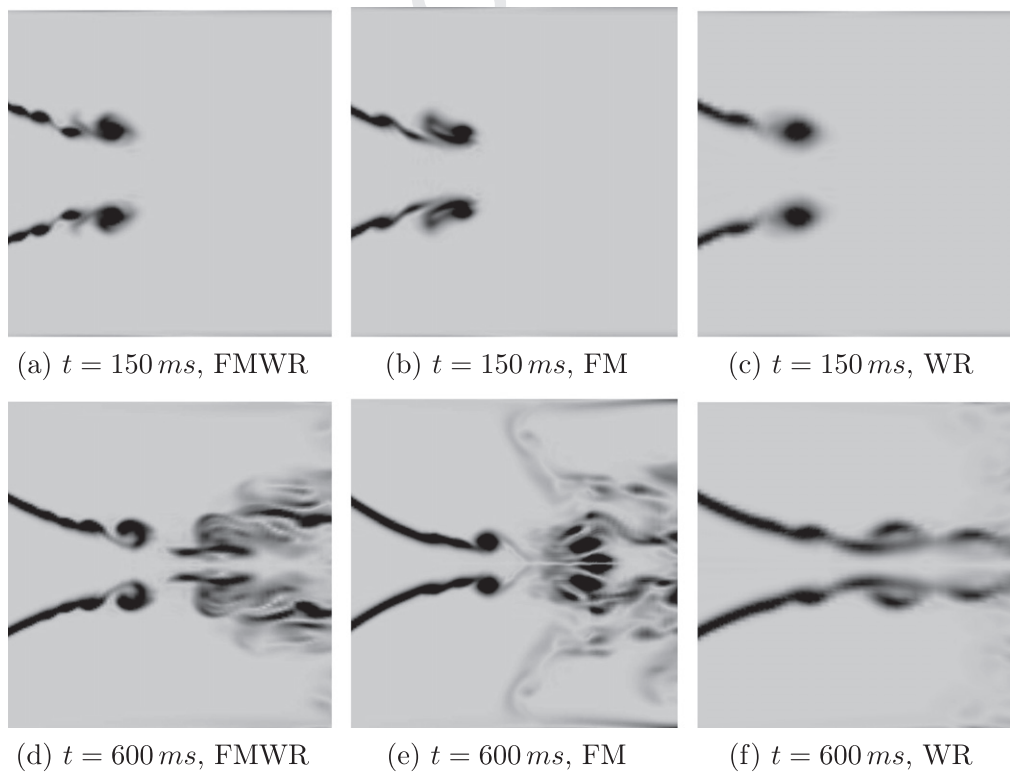


Fig. 10. Flow resolution in major plane with the CFD model on different numerical grids, indicated by $\|\Omega_y\|$ with the scale in Fig. 7c.

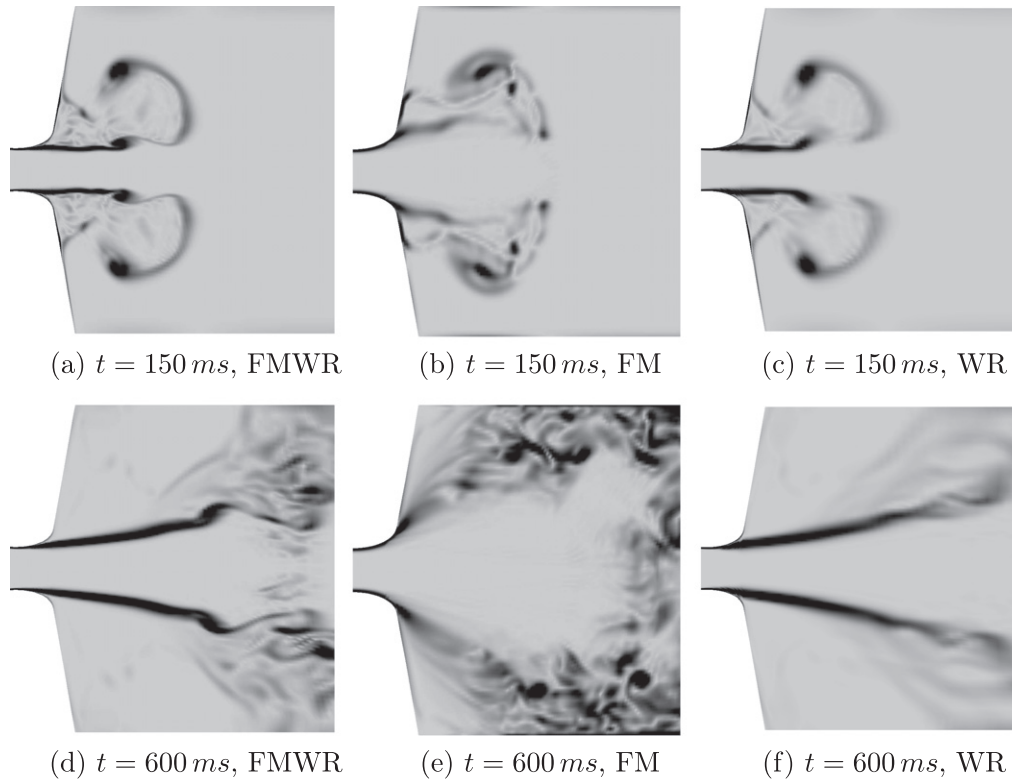


Fig. 11. Flow resolution in minor plane with the CFD model on different numerical grids, indicated by $\|\Omega_z\|$ with the scale in Fig. 7c.

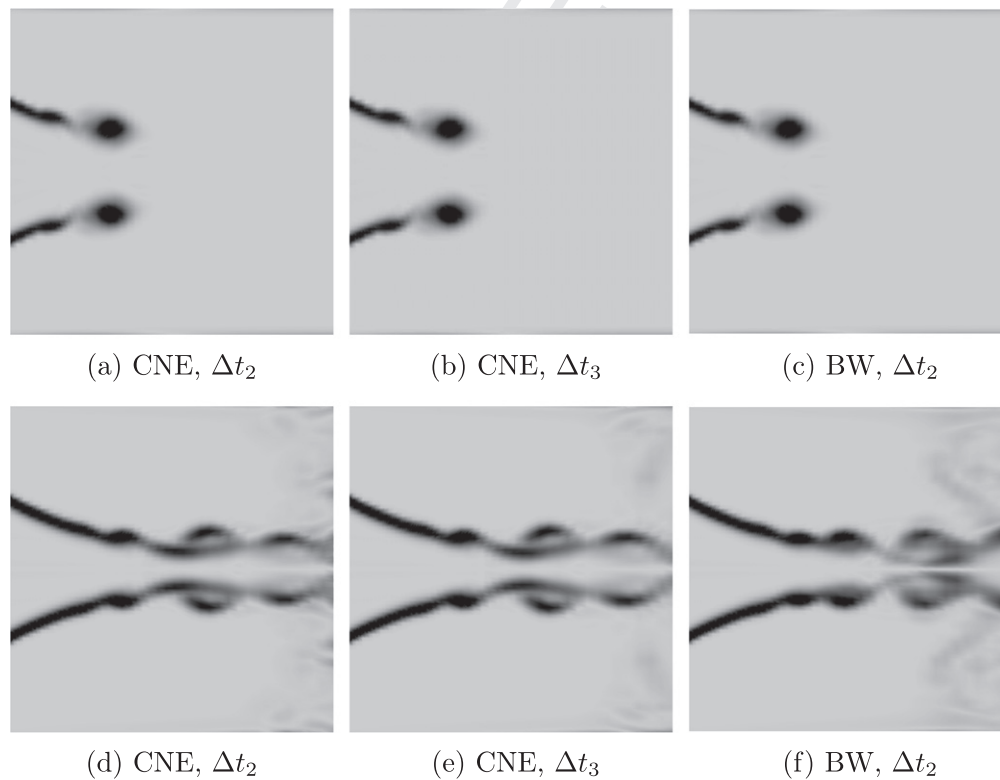


Fig. 12. Influence of time integration scheme and time-step width on the flow resolution in major plane on grid WR, indicated by $\|\Omega_y\|$ with the scale in Fig. 7c, first row: $t = 300 \text{ ms}$, second row: $t = 600 \text{ ms}$.

the numerical results of FMWR and WR, and both data sets differ noticeably to the PIV measurements. Obviously, the results on grid

FMWR and WR are not in phase, whereas the amplitudes and lengths of the wave trains are similar on both grids.

427
428

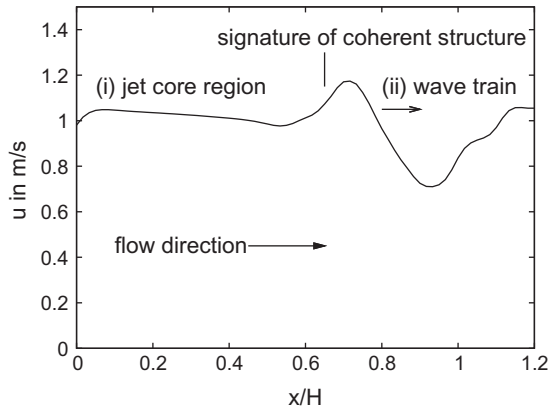


Fig. 13. Velocity profile $u(x/H)$ from CFD model on grid FMWR at $t = 450$ ms along baseline P1 (x -axis).

On the contrary, the numerical results of grid FM exhibit more pronounced differences in both the phases and the amplitudes with respect to the numerical data of the other grids and the PIV measurements. Especially the jet core velocity is underpredicted immediately downstream of the glottis, which is a consequence of the stronger deceleration of the jet flow in this region, see Fig. 9.

Fig. 15 also correlates the numerical and experimental velocity profiles at baseline P1, but here the numerical simulations are carried out with four different time-step sizes ($\Delta t_1 \dots \Delta t_4$) and two

different integration schemes (CNE, BW) on the same grid (WR). Obviously, the results of case WR, CNE in Fig. 15a show convergent behavior for decreasing time-step width. The differences between $\Delta t_2, \Delta t_3$ and Δt_4 are only marginal at the end of the simulation period at $t = 600$ ms. Here only the results of the simulation with the largest time-step width Δt_1 differ noticeable in phase and magnitude. The results of case WR, BW in Fig. 15b show the same tendency, but here velocity profiles in the simulations with Δt_1 and Δt_2 differ from the corresponding profiles for Δt_3 and Δt_4 .

Fig. 16 shows the influence of the grid and the time integration scheme on the simulation results. Obviously, there is a good agreement of the profiles on grid WR for simulations with BW ($\Delta t_3, \Delta t_4$) and CNE ($\Delta t_2, \Delta t_3, \Delta t_4$), see Fig. 16a. On the other hand, the differences between the two grids FMWR and WR for simulations with a fixed time integration scheme are nearly independent from the time-step size of the simulation, see Fig. 16b. Therefore, we conclude that convergence of the results from different grids cannot be achieved, whereas the influence of the time integration scheme is of minor importance for the simulation results.

Nevertheless we assume that the characteristic change of the velocity profile for $x/H > 0.6$ is primarily due to the transitional and nonlinear behavior, whereas the numerical resolution has only a minor impact on the characteristic shape of the profile. The transition is introduced to the flow by the two touching shear layers at $x/H \approx 0.6$ and small numerical fluctuations are strongly amplified downstream of this point. Because these numerical fluctuations are different on grids FMWR and WR, distinct specific amplitudes are observed on these grids. In the experiments, a corresponding

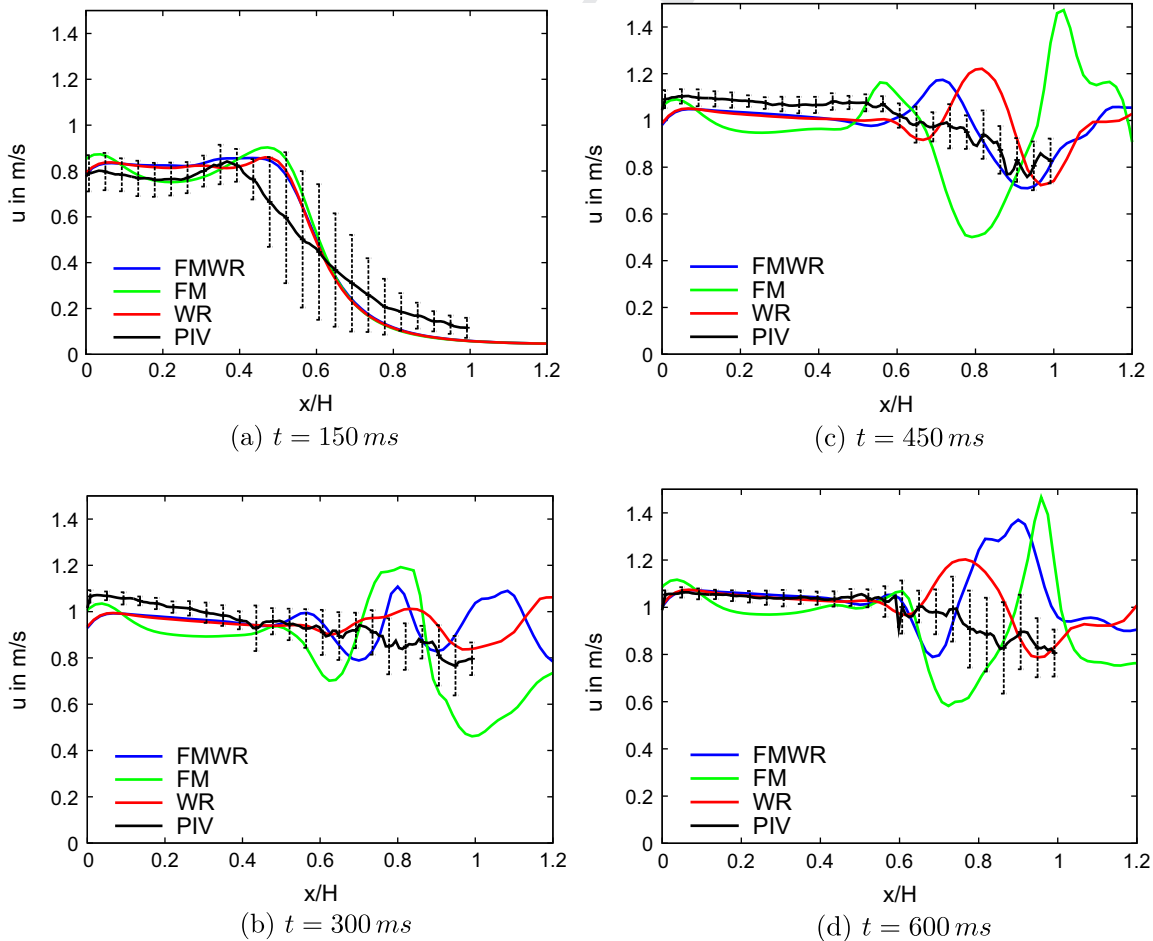


Fig. 14. Development of $u(x/H)$ along along baseline P1 (x -axis), comparison of PIV measurement and CFD model results from simulation with CNE and Δt_i .

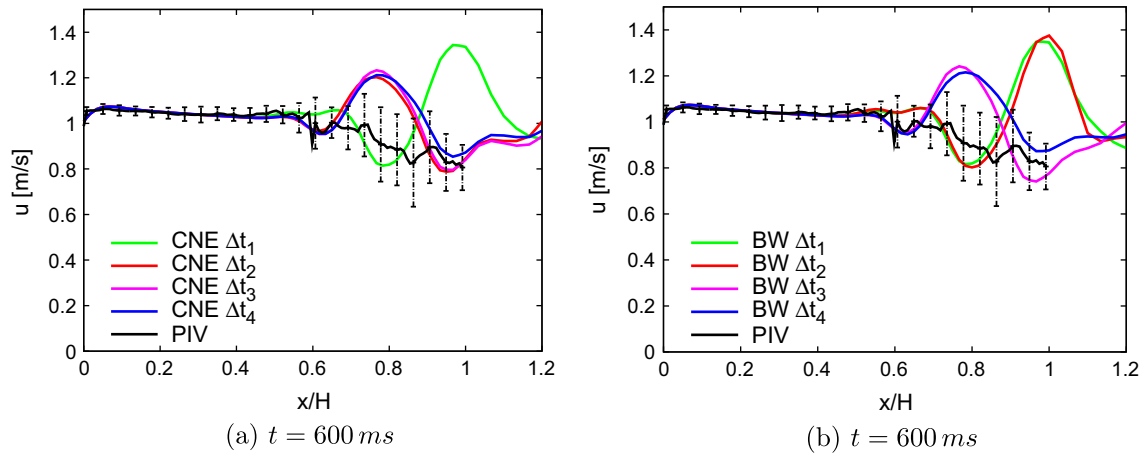


Fig. 15. Development of $u(x/H)$ along baseline P1 (x -axis), comparison of PIV measurements and simulation results on grid WR with CNE and BW and different time-step sizes, respectively.

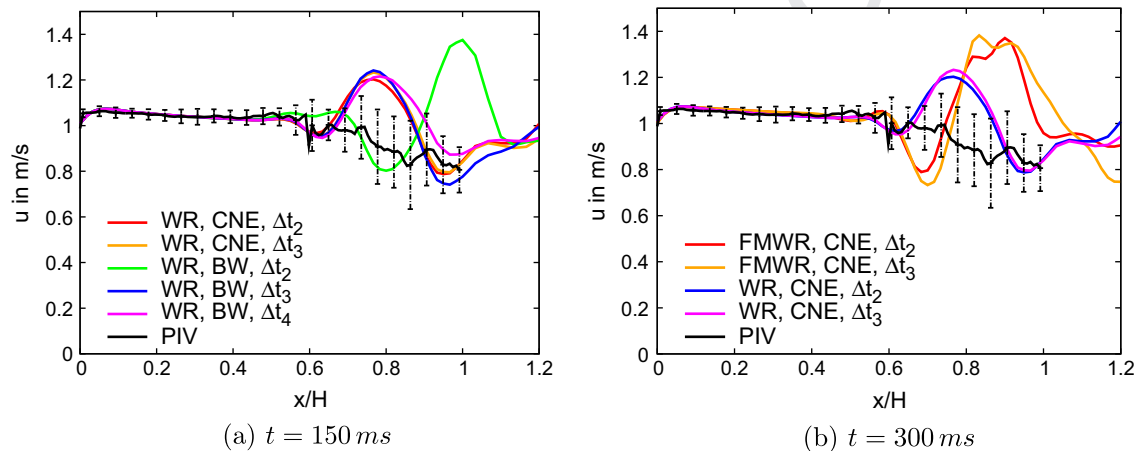


Fig. 16. Development of $u(x/H)$ along baseline P1 (x -axis), comparison of simulation results for different grids and different time discretization, respectively.

466 transition is indicated by the increasing rms values for $x/H \approx 0.6$,
467 see e. g. sub Figs. 14c and d.

468 Fig. 17 gives an estimation of the mean-square error, which re-
469 sults from amplification of the small numerical disparities. Here,
470 the averaged results from the numerical simulations (SIM) from
471 eight different cases (grids FMWR and WR with integration
472 schemes CNE and BW for time-step sizes Δt_2 and Δt_3 , respectively)
473 with their mean deviations are compared with the ensemble-aver-
474 aged PIV measurements. Obviously the spreading of the numerical
475 results, which is observed only for $x/H \geq 0.6$, increases with time.
476 Again, the overall agreement between SIM and PIV is acceptable.
477 However we admit that the numerical data set is not really an
478 ensemble in a physical sense, therefore the interpretation of
479 Fig. 17 must be done carefully.

480 Fig. 18 compares the numerical and experimental velocity pro-
481 files $u(y/H)$ at baseline P2 near to the glottis for two different flow
482 times t . Note that spurious leakage currents have been observed in
483 the experiment near the upper and lower wall which are due to
484 non-perfect contact of the ceiling. The figures show typical jet pro-
485 files with the high velocity jet core region around $y/H = 0$, steep jet
486 shear layers approximately at $y/H \approx \pm 0.1$ and the ambient fluid at rest.
487 The numerical simulations on grids FMWR and WR fit again
488 well to the experimental measurements in both subfigures. Here
489 the numerical simulation on grid FM clearly underpredicts the jet
490 core velocity, whereas the width of the jet is drastically
491 overpredicted.

492 Fig. 19 compares the numerical and experimental velocity pro-
493 files $u(z/H)$ at baseline P3 for two different flow times t . Again,
494 leakage currents are observed in the experiment. The figures show
495 again typical features of jet profiles, the high velocity jet core re-
496 gion around $z/H = 0$ and steep jet shear layers approximately at
497 $z/H \approx \pm 0.1$. As in Fig. 18, the numerical simulations on grids FMWR
498 and WR fit well to the experimental measurements in both subfig-
499 ures. Here the numerical simulation on grid FM gives a good reso-
500 lution of the jet profile for $t = 150$ ms, but at $t = 600$ ms, the jet core
501 velocity and the width of the jet are again underpredicted.

502 In summary, we expect, that our numerical model with proper
503 chosen time discretization will give a reasonable description of the
504 dynamics of large coherent structures in the developing flow.
505 Velocity amplitudes and characteristic length scales of the struc-
506 tures should be sufficiently resolved in order to understand the basic
507 features of the vortex kinematics and dynamics. However, a
508 more detailed inspection of the fine scale interactions in the inter-
509 mediate vortex field would demand a refined numerical model.

3.3. Near glottis flow

3.3.1. Glottal boundary layer

511 When the flow is accelerated through the glottis, laminar
512 boundary layers develop at the vocal folds. Fig. 20 gives details of
513 the boundary layers at $x = 0, z = 0$, where profiles of $u/u_{max}(y^+)$
514 are given along the minor (y) axis of the glottis. Here y^+ is deter-
515

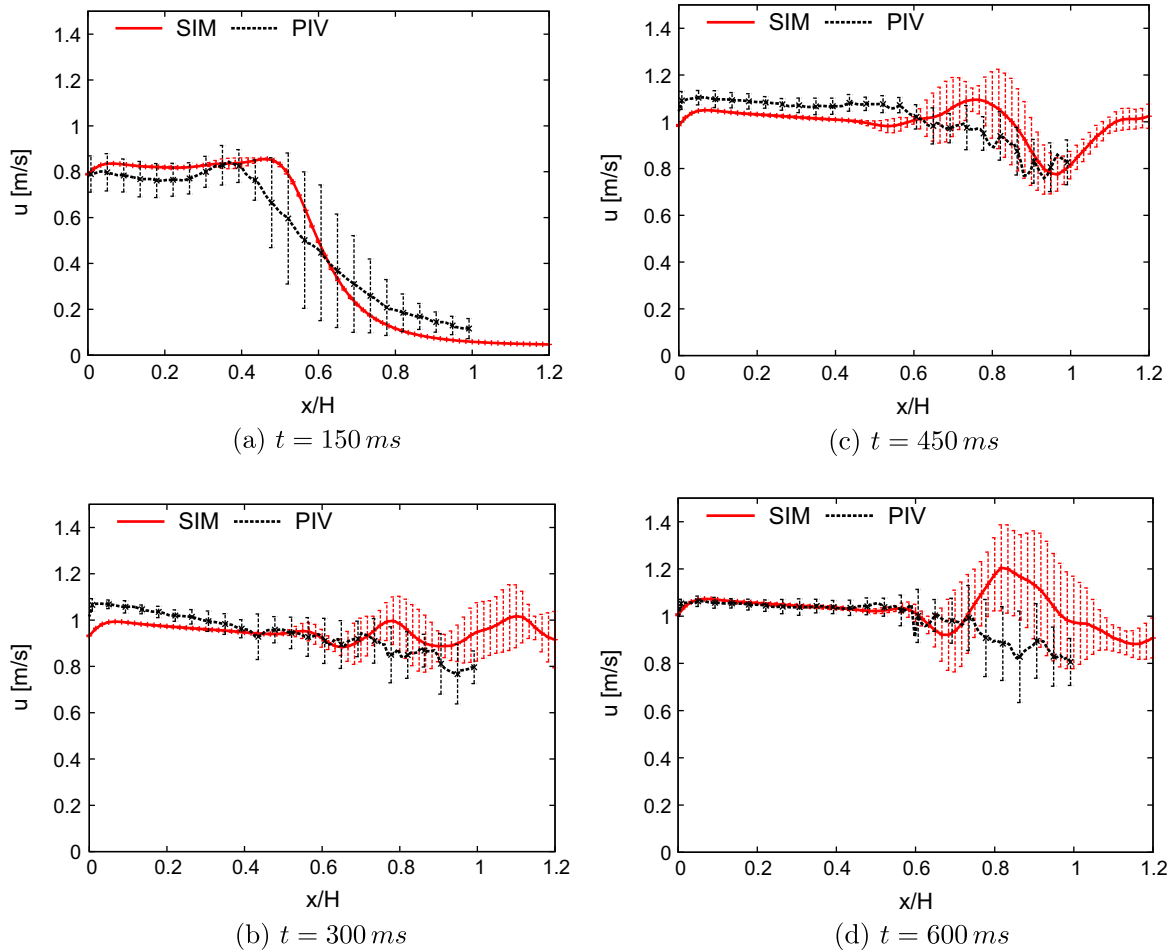


Fig. 17. Development of $u(x/H)$ along baseline P1 (x -axis), comparison of ensemble-averaged PIV measurements and averaged simulation results (SIM).

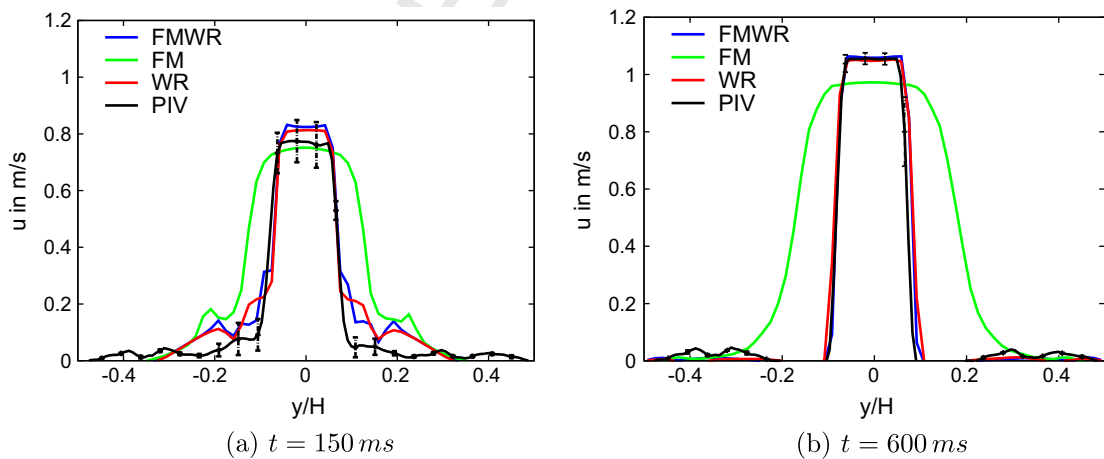


Fig. 18. Development of $u(y/H)$ along baseline P2, comparison of PIV measurement with CFD model results from simulations with CNE and Δt_2 .

516 with the instantaneous local wall shear stresses τ_w at the glottis
517 and u/u_{max} is referred to the instantaneous maximum velocity u_{max}
518 which is observed in the glottis.

519 Obviously, shear layer profiles are resolved nearly identically on
520 both grids FMWR and WR (starting at $y_{min}^+ \simeq 2$ in the center of the
521 wall-nearest cell). PIV measurements are not possible in this region

522 of the experiment, therefore a comparison with experimental data
523 cannot be given.

524 In Fig. 20, the linear profile $(u/u_{max})_{lin} = 0.0764 y^+$ is also indicated
525 as a dashed line starting at $y^+ = 0$. The comparison of the linear
526 and the FS profile reveals a point of inflexion near $y^+ \simeq 2$, which
527 suggests that the flow downstream of the glottis will become crit-

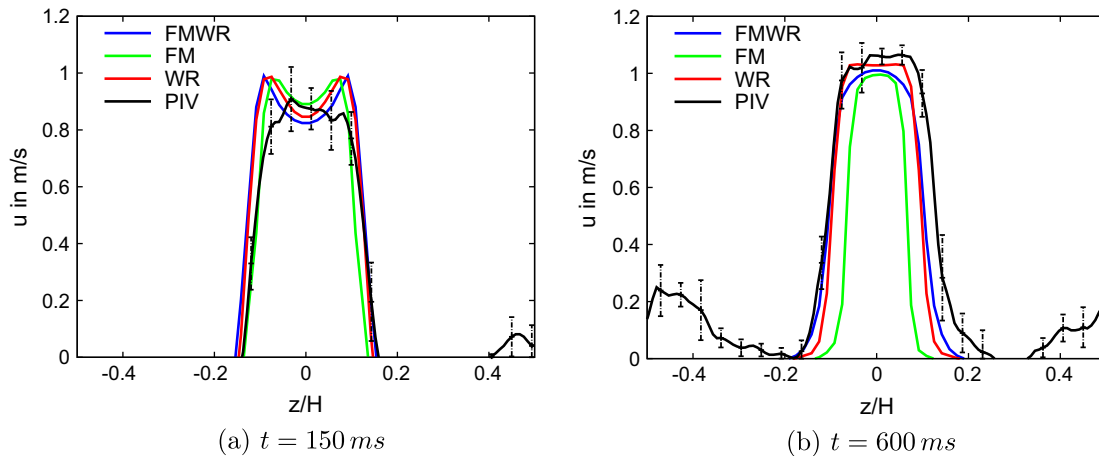


Fig. 19. Development of $u(z/H)$ along baseline P3, comparison of PIV measurement with CFD model results from simulations with CNE and Δt_2 .

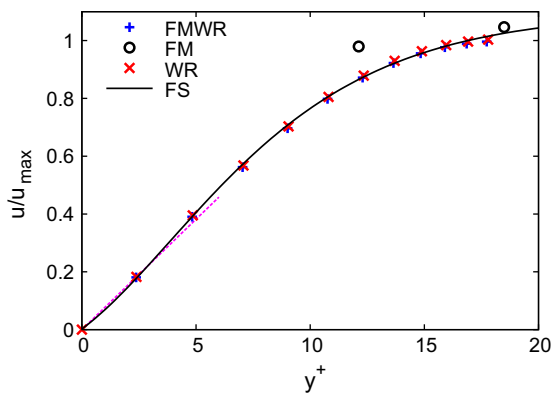


Fig. 20. Boundary layer $u/u_{max}(y^+)$ along minor axis at $x=0, z=0$ (in the smallest cross section of the glottis).

ical for separation, because $d(u/u_{max})/dy^+ \rightarrow 0$ for $y^+ = 0$. Additionally, the separated free shear layer is prone to transitional behavior due to the point of inflexion.

Although we have no possibility to give a validation by comparison with experimental data, we are convinced that the boundary layer is sufficiently resolved by the numerical grids FMWR and WR. The important scale, i.e. the boundary layer thickness is similar on both grids. The slight deviation between the profile slopes seems to be due to the different resolution of the jet core regions, which have to be matched at the outer boundary layers.

On the contrary, the resolution of the shear layer profile on grid FM is inappropriate (it starts with $y_{min}^+ = 12$ in the center of the wall-nearest cell). Therefore, results from grid FM are no longer discussed in the paper.

3.3.2. Flow separation

At some distance downstream of the smallest cross section, the boundary layers separate from the vocal folds. The separation line on the lower vocal fold is investigated in Fig. 21. Due to the acceleration of the boundary layer, the location of the separation line is determined using the MRS criterion for the streamwise velocity u_s , i.e. $\partial u_s / \partial n = 0$ at $u_s = 0$ [38].

The resolution of the separation line on grids WR and FMWR is nearly identical, only small differences (below 1% with respect to D) are observed, see Fig. 21. At the touching vocal folds, the boundary layers separate immediately from the contour, whereas in the center line of the vocal fold, the separation occurs further downstream at $x/H \approx 0.05$. The profile shows two additional bumps in the vicin-

ity of the touching vocal folds at $z/D = \pm 0.04$, which indicate a localized shifting of the separation. This shifting originates from the inward directed displacement of the flow due to the touching vocal folds, which adds momentum to the boundary layer at these points.

The time integration scheme and the time-step width have no observable influence of the resolution of the separation line on a specific grid, see Fig. 21b. Here, the results from simulations with CNE and BW with Δt_3 and Δt_4 show only negligible differences.

3.4. Glottal Jet

3.4.1. Leading vortex

Similar to starting round jets, the starting jet flow which develops downstream of the glottis consists of a leading vortex and a trailing jet, see Fig. 7. We apply the method described in [16,17] in order to study the formation of the leading vortex in more detail. The leading vortex is detected by the inspection of the isocontours in the vorticity fields in the major, see Fig. 22. The leading vortex and the trailing shear layers are indicated by high values of vorticity, but these structures are separated by a region of lower vorticity, which is clipped in the figure.

The total circulation Γ_{tot} is calculated by integrating the vorticity in the entire major plane. The circulation of the leading vortex Γ_{lv} is estimated by integrating the vorticity inside an isocontour of vorticity that includes the leading vortex. Although this procedure is carried out to the best of our judgement, the evaluation of the vortex circulation is more subjective, especially before a clear pinch-off can be observed.

Fig. 23 shows Γ_{tot} and Γ_{lv} which is found in the major plane. Both simulations on grids FMWR and WR give nearly the same slopes of Γ_{tot} and Γ_{lv} . Γ_{tot} increases nearly uniformly due to the continuous entrainment of the separated boundary layers as free shear layers into the flow domain. Contrary Γ_{lv} is found to be constant for $9 \leq t^* \leq 15$. Then, a slight increase of Γ is observed for $t^* > 15$, but there is also an increasing uncertainty in these values. Due to the increasing complexity of the structure of the leading vortex, the determination of Γ becomes more and more difficult. Finally, we cannot specify reliable values for Γ for $t^* > 20$.

According to Gharib et al. [16], the separation of the leading vortex is determined by extrapolation from the curve of Γ_{lv} . The separation of the leading vortex from the trailing jet is expected at a dimensionless formation time or formation number $t^* = U_m \times t / d_{jet} \sim 5$ with $U_m(t) = 1/t \int_0^t u^{in}(t) dt$. A similar investigation of Γ_{tot} and Γ_{lv} in the minor planes confirms this result, which is also in agreement with the findings of Gharib et al. [16] for round jets.

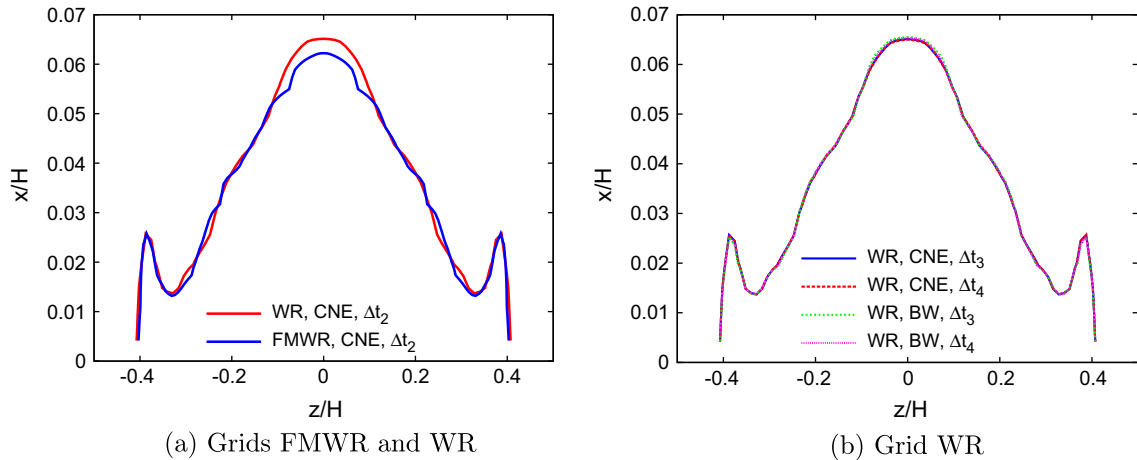


Fig. 21. Location of the separation lines at the lower vocal fold for $t = 450$ ms (top view on the vocal fold).

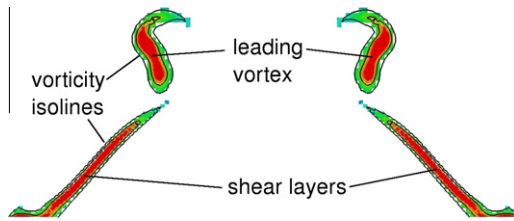


Fig. 22. Detection of the leading vortex: vorticity field in the major plane on grid FMWR, colored are regions with vorticity $\|\Omega_z\| \geq 200 \text{ s}^{-1}$, blue colors indicate low values, red colors indicate high values of the vorticity, flow direction is from bottom to top. (For interpretation of the references to color in this figure legend, the reader is referred to the web version of this article.)

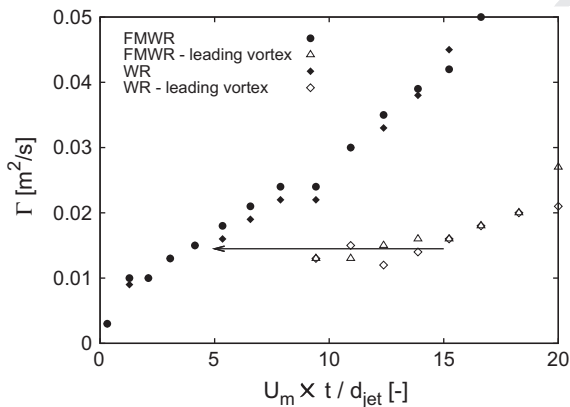


Fig. 23. Circulation Γ in the major plane as a function of dimensionless formation time $U_m \times t / d_{jet}$ on grids FMWR and FM, black symbols give the total circulation, open symbols give the circulation of the leading vortex, $U_m \times t / d_{jet} = 10$ corresponds to flow time $t = 95$ ms.

3.4.2. Vortex kinematics and dynamics

The development of the vortex field in the starting glottal jet flow is illustrated in Fig. 24. In the figures characteristic vortex structures in the transient flow are visualized by the Q criterion [37]. Here, isosurfaces with $Q = 10^4$ are colored with the local relative pressure, which is given with respect to ambient pressure. Obviously the leading vortex induces a marked pressure drop in the flow, Fig. 24a, whereas the secondary vortices which develop in the shear layers of the trailing jet do not exhibit a noticeable underpressure. During the transient development, the vortices

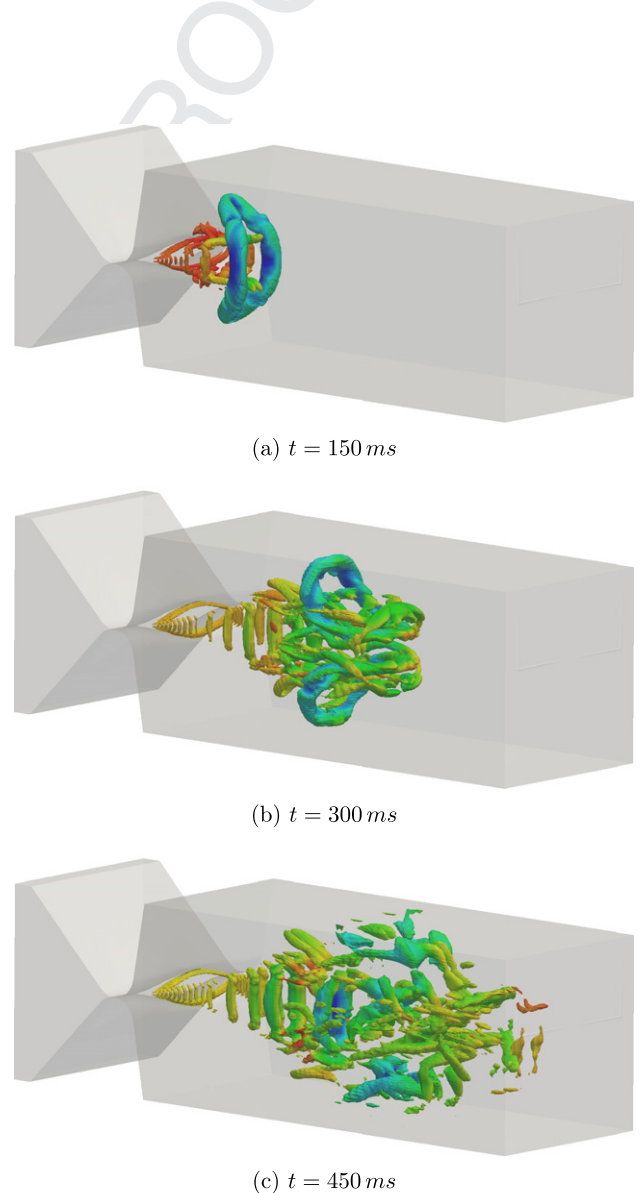


Fig. 24. Vortical flow structures of the starting supraglottal jet, visualized by the Q criterion with isosurfaces $Q = 10^4$. Isosurfaces are color-coded with relative pressure p (blue is $p = -200$ Pa, red is $p = 0$ Pa) with respect to ambient pressure. (For interpretation of the references to color in this figure legend, the reader is referred to the web version of this article.)

600
601
602
603
604
605
606
607
608
609

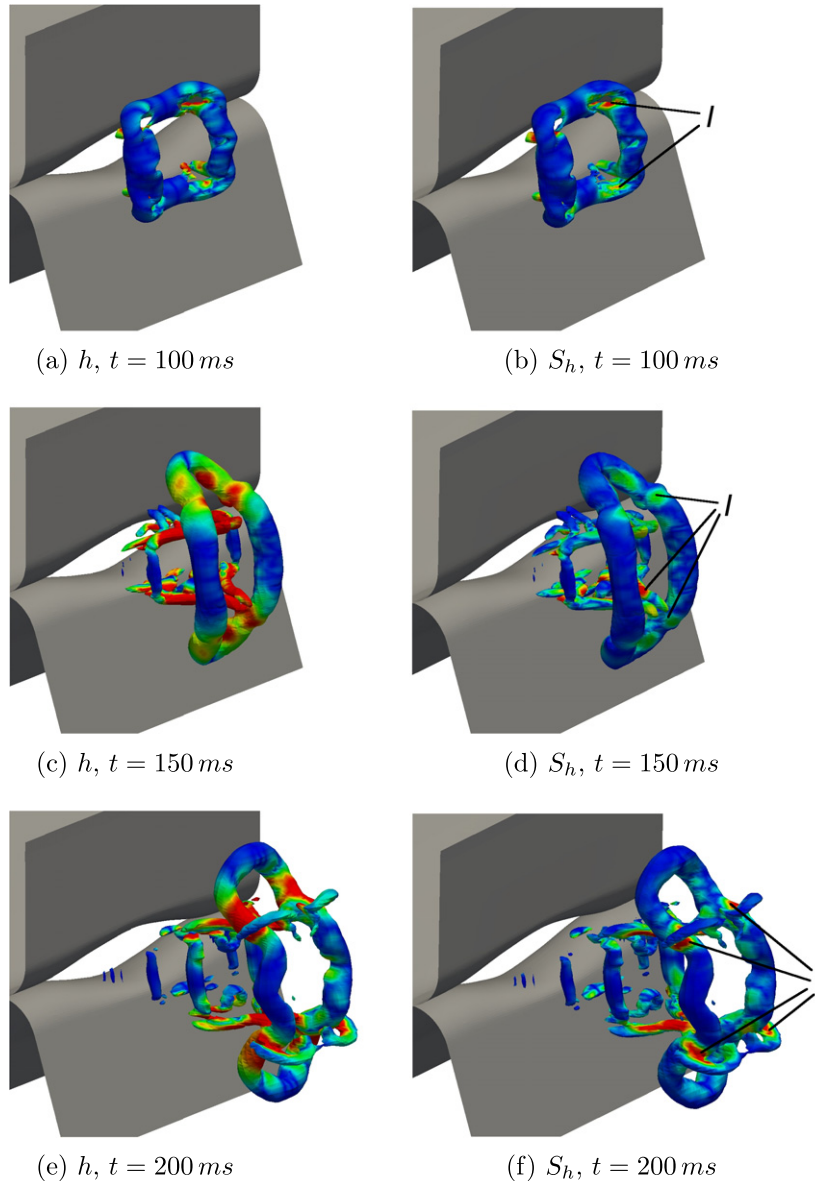


Fig. 25. Vortical flow structures of the starting supraglottal jet, visualized by the Q criterion with isosurfaces $Q = 10^4$. Isosurfaces are color-coded with magnitude of helicity density $\|h\|$ (blue is $\|h\| = 0$, red is $\|h\| = 100 \text{ m/s}^2$) or with magnitude of source $\|S_h\|$ of h (blue is $\|S_h\| = 0$, red is $\|S_h\| = 5 \cdot 10^4 \text{ m/s}^3$), respectively. (For interpretation of the references to color in this figure legend, the reader is referred to the web version of this article.)

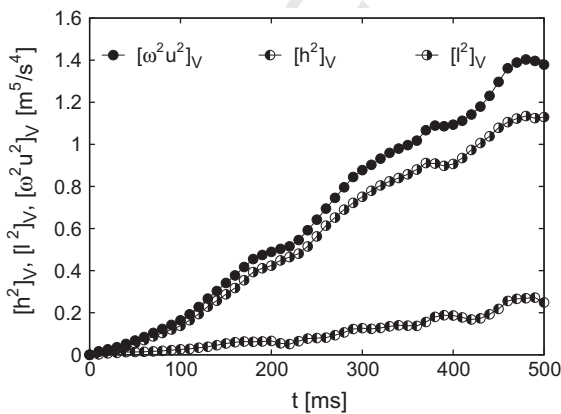


Fig. 26. Volume integrals $[\Omega^2 u^2]_V$, $[h^2]_V$ and $[l^2]_V$ as a function of t .

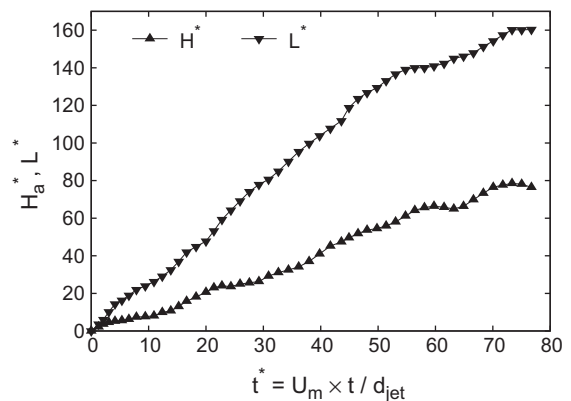


Fig. 27. Dimensionless absolute helicity H_a^* and Lamb vector integral L^* as a function of t^* .

interact strongly, Fig. 24b and c, whereby the pressure drop in the flow is somewhat smoothed.

The dynamics of the developing glottal jet and the interactions between the jet and the leading vortex can be analyzed in more detail by the investigation of the helicity density $h = \underline{\Omega} \cdot \underline{u}$. We use h as an indicator for the relationship between the directions of flow and rotation. We expect that a change of h will be a sign of the interaction between vortices. In the incompressible flow, h obeys [39,40]

$$\frac{\partial h}{\partial t} = \frac{\partial}{\partial x_i} \left[-h u_i + \left(\frac{u_j^2}{2} - \frac{p}{\rho} \right) \Omega_i + \nu \frac{\partial h}{\partial x_i} \right] - 2\nu \frac{\partial u_j}{\partial x_i} \frac{\partial \Omega_j}{\partial x_i} \quad (3)$$

We have investigated both h and its source terms S_h , i.e. the right-hand side of Eq. (3) in the flow. As an example, Fig. 25 shows the organized vortex structures in the near-glottis region transient flow, which are again resolved by the Q criterion. Here, the isosurfaces of Q are colored with $\|h\|$ and $\|S_h\|$, respectively. Clearly, high values of $\|S_h\|$ are observed in the regions, where the leading vortex interacts with secondary vortices, which develop from the shear layers of the trailing jet. Some of these localized regions are indicated by I in Figs. 25b, d and f. Consequently, the total amount of helicity density increases due to the positive source terms, as it is observed in Figs. 25a, c and e.

The helicity density together with the Lamb vector $\underline{l} = \underline{\Omega} \times \underline{u}$ give a local orthogonal decomposition of \underline{u} with respect to $\underline{\Omega}$. Both h and \underline{l} are related to the product of twice the specific kinetic energy $\underline{u}^2/2$ and the enstrophy $\underline{\Omega}^2$ by

$$\underline{\Omega}^2 \underline{u}^2 = |h|^2 + |\underline{l}|^2 \quad (4)$$

$$\int_V \underline{\Omega}^2 \underline{u}^2 dV = \int_V |h|^2 dV + \int_V |\underline{l}|^2 dV \quad (5)$$

Fig. 26 gives the development of $[\underline{\Omega}^2 \underline{u}^2]_V$, $[h^2]_V$ and $[|\underline{l}|^2]_V$ for the accelerating phase in the entire flow volume downstream of the glottis. It is found that $[\underline{\Omega}^2 \underline{u}^2]$ is divided with a ratio of approximately 1:4 between h and \underline{l} . This underlines that the dynamics of the starting glottal jet has a three-dimensional nature. The helicity density, which is zero in two-dimensional and axisymmetric flow fields seems to play an important role in the physics of the glottal jet.

Fig. 27 underlines this conclusion. Here, the absolute helicity, i.e. the volume integral of the helicity magnitude $H_a = \int_V |h| dV$ and $L = \int_V |\underline{l}| dV$ are given. Based on the findings of Moffatt [41], see also [42], H_a is a measure for the knotness of the vorticity lines in a flow region V . Therefore the increase of H_a should indicate an increase of the strengths and the winding numbers of the vortex structures in the flow. In Fig. 27, H_a^* and L^* are given in dimensionless form based on U_m and d_{jet} . Again, the important increase of H_a^* demonstrates that the three-dimensional vortex interactions induce an increase of the streamwise-oriented vorticity. The scaling which was found from the empirical fit of the data is $H_a^* \sim t^*$ and $L^* \sim (t^*)^{0.8}$, the corresponding curves are also indicated in Fig. 27.

4. Summary and outlook

A numerical model of starting supraglottal jet flows is presented. The model is based on the equation of continuity and the Navier–Stokes equations for incompressible flows. Transient simulations of the starting jet flows in the supraglottal channel are carried out. The geometry, boundary conditions and initial values of the flow fit to a corresponding model experiment which is discussed elsewhere.

The numerical model is implemented into the open source code OpenFOAM. As discretization schemes, the combination of a

second-order TVD scheme and a blended Crank–Nicolson and Euler implicit scheme are employed for flux interpolation and time integration, respectively. The numerical setup is assumed to realize a blending between a direct computation of the laminar flow regions and an implicit Large-Eddy Simulation for the transitional and the turbulent flow regions.

Qualitative and quantitative comparison of numerical and experimental data show, that the numerical model is able to resolve the flow field correctly. A grid variant study shows, that the near-wall grid resolution should be fine enough in order to resolve the flow separation and the corresponding jet development adequately.

The simulations give detailed insight into the structure of the developing flow field, which is composed of the glottal region, the leading vortex and the trailing jet flow. Boundary layer profiles of the flow in the glottis, the separation line on the vocal folds, velocity profiles of the jet flow and the jet flow region are analyzed.

The boundary layers in the glottal flow region are similar to the boundary layers of the flow through a wedge nozzle. The separation line of the jet flow from the diverging vocal folds remains nearly constant throughout the transient development of the flow.

The large coherent vortex structures of the trailing jet interact strongly with the leading vortex, which is indicated by a marked rise of helicity density during the jet development. Both the Lamb vector integral and the helicity in the supraglottal flow region are found to increase nearly constantly over the complete starting period of the jet flow.

Future studies should be focused on the following topics:

- Realistic flow rate functions should be applied. The focus of the present study is to develop a suitable numerical model for three-dimensional simulations of supraglottal jet flows and to resolve basic structures and transition processes in these flows. Therefore, long-term simulations with oscillating flow rates should be an interesting continuation of our work. In this context, dynamic grids should be implemented which model the oscillating movement of the vocal folds.
- The development of the Lamb vector and the helicity should be analyzed in more detail because of the importance of the Lamb vector for the acoustics of the glottal jet.
- The flow simulations should be coupled to calculations of the acoustic field in order to analyze the process of sound generation in more detail. Here, as a first step, the acoustic source terms must be deduced from the flow data.

Acknowledgements

The authors thank the German Science Foundation DFG for funding the research under Grant No. BR 1494/13-1.

References

- [1] Sciamarella D, Le Quere P. Solving for unsteady airflow in a glottal model with immersed moving boundaries. *Eur J Mech B/Fluids* 2008;27:42–53.
- [2] Alipour F, Scherer RC. Flow separation in a computational oscillating vocal fold model. *J Acoust Soc Am* 2004;116:1710–9.
- [3] Decker GZ, Thomson SL. Computational simulations of vocal fold vibration: Bernoulli versus Navier–Stokes. *J Voice* 2007;21:273–84.
- [4] Tao C, Zhang Y, Hottinger DG, Jiang JJ. Asymmetric airflow and vibration induced by the Coanda effect in a symmetric model of the vocal folds. *J Acoust Soc Am* 2007;121:2270–8.
- [5] Suh J, Frankel SH. Numerical simulation of turbulence transition and sound radiation for flow through a rigid glottal model. *J Acoust Soc Am* 2007;121:3728–39.
- [6] Li S, Scherer RC, Wan MX, Wang SP, Wu HH. Numerical study of the effects of inferior and superior vocal fold surface angles on vocal fold pressure distributions. *J Acoust Soc Am* 2006;119:3003–10.

- [7] Duncan C, Zhai G, Scherer RC. Modeling coupled aerodynamics and vocal fold dynamics using immersed boundary methods. *J Acoust Soc Am* 2006;120:2859–71.
- [8] Bae Y, Moon YC. Computation of phonation aeroacoustics by an INS/PCE splitting method. *Comput Fluids* 2008;37:1332–43.
- [9] Zheng X, Bielamowicz S, Luo HX, Mittal R. A computational study of the effect of false vocal folds on glottal flow and vocal fold vibration during phonation. *Ann Biomed Eng* 2009;37:625–43.
- [10] Larsson M, Müller B. Numerical simulation of confined pulsating jets in human phonation. *Comput Fluids* 2009;38:1375–83.
- [11] Triep M, Brücker Ch, Schröder W. High-speed PIV measurements of the flow downstream of a dynamic mechanical model of the human vocal folds. *Exp Fluids* 2005;39:232–45.
- [12] Neubauer J, Zhang Z, Miraghaie R, Berry DA. Coherent structures of the near field flow in a self-oscillating physical model of the vocal folds. *J Acoust Soc Am* 2007;121:1102–18.
- [13] Drechsel JS, Thomson SL. Influence of supraglottal structures on the glottal jet exiting a two-layer synthetic, self-oscillating vocal fold model. *J Acoust Soc Am* 2008;123:4434–45.
- [14] Renotte C, Bouffieux V, Wilquem F. Numerical 3D analysis of oscillatory flow in the time-varying laryngeal channel. *J Biomech* 2000;33:1637–44.
- [15] Brouns M, Verbanck S, Lacor C. Influence of glottic aperture on the tracheal flow. *J Biomech* 2007;40:165–72.
- [16] Gharib M, Rambod E, Shariff K. A universal time scale for vortex ring formation. *J Fluid Mech* 1998;360:121–40.
- [17] Rosenfeld M, Rambod E, Gharib M. Circulation and formation number of laminar vortex rings. *J Fluid Mech* 1998;376:297–318.
- [18] Shusser M, Gharib M. Energy and velocity of a forming vortex ring. *Phys Fluids* 2000;12:618–21.
- [19] Mohseni K, Ran H, Colonius T. Numerical experiments on vortex ring formation. *J Fluid Mech* 2001;430:267–82.
- [20] Krueger PS, Gharib M. The significance of vortex ring formation to the impulse and thrust of a starting jet. *Phys Fluids* 2003;15:1271–81.
- [21] Gao L, Yu SCM. A model for the pinch-off process of the leading vortex ring in a starting jet. *J Fluid Mech* 2010;656:205–22.
- [22] Margolin LG, Rider WJ, Grinstein FF. Modeling turbulent flows with implicit LES. *J Turbul* 2006;7:1–27.
- [23] Grinstein FF, Margolin LG, Rider WJ. Implicit large eddy simulation. New York: Cambridge University Press; 2007.
- [24] Grinstein FF, DeVore CR. Dynamics of coherent structures and transition to turbulence in free square jets. *Phys Fluids* 1996;8:1237–51.
- [25] Drikakis D, Fureby C, Grinstein FF, Hahn M, Youngs D. LES of transition to turbulence in the Taylor Green vortex. In: Proceedings of 6th International ERCOFTAC Workshop on Direct and Large-Eddy Simulation. Dordrecht (NL): Springer; 2006. p. 159–66.
- [26] OpenCFD Ltd. OpenFOAM 1.5 documentation. <<http://www.open CFD.co.uk/openfoam/doc/index.html>>.
- [27] van Leer B. Towards the ultimate conservative difference scheme. V. A second-order sequel to Godunov's method. *J Comput Phys* 1979;32:101–36.
- [28] Fureby C. ILES and LES of complex engineering turbulent flows. *J Fluids Eng* 2007;129:1514–23.
- [29] Grinstein FF, Fureby C, DeVore CR. On MILES based on flux-limiting algorithms. *Int J Numer Methods Fluids* 2005;47:1043–51.
- [30] Issa RI. Solution of the implicit discretized fluid flow equations by operator splitting. *J Comp Phys* 1985;62:40–65.
- [31] Rhie CM, Chow LW. Numerical study of the turbulent flow past an airfoil with trailing edge separation. *AIAA J* 1983;21:1525–32.
- [32] Fletcher RW. Conjugate gradient methods for indefinite systems. *Lect Notes Math* 1976;506:73–89.
- [33] Karypis G, Kumar V. A fast and high quality multilevel scheme for partitioning irregular graphs. *SIAM J Sci Comp* 1999;20:359–92.
- [34] Karypis G, Kumar V. METIS 4.0 documentation. <<http://glaros.dtc.umn.edu/gkhome/metis/metis/download>>.
- [35] Hussain F, Hussain HH. Elliptic jets. Part 1. Characteristics of unexcited and excited jets. *J Fluid Mech* 1989;208:257–320.
- [36] Hussain HH, Hussain F. Elliptic jets. Part 2. Dynamics of coherent structures: pairing. *J Fluid Mech* 1991;233:439–82.
- [37] Jeong J, Hussain F. On the identification of a vortex. *J Fluid Mech* 1995;285:69–94.
- [38] Schlichting H, Gersten K. Boundary layer theory. Berlin: Springer; 2003.
- [39] Yoshizawa A. Hydrodynamic and magnetohydrodynamic turbulent flows. Dordrecht: Kluwer; 1998.
- [40] Holm DD, Kerr RM. Helicity in the formation of turbulence. *Phys Fluids* 2007;19:025101.
- [41] Moffatt HJ. The degree of knottedness of tangled vortex lines. *J Fluid Mech* 1969;35:117–29.
- [42] Wu JZ, Ma HY, Zhou MD. Vorticity and vortex dynamics. Berlin: Springer; 2006.

771
772
773
774
775
776
777
778
779
780
781
782
783
784
785
786
787
788
789
790
791
792
793
794
795
796
797
798
799
800
801
802
803
804
805
806
807
808
809
810